



Cite this: DOI: 10.1039/d0lc00725k

Nondestructive quantification of single-cell nuclear and cytoplasmic mechanical properties based on large whole-cell deformation†

 Jifeng Ren,^a Yongshu Li,^b Shuhuan Hu,^{acd} Yi Liu,^a Sai Wah Tsao,^e Denvin Lau,^f Guannan Luo,^g Chi Man Tsang^{*b} and Raymond H. W. Lam^{id} ^{*ahi}

The mechanical properties of cell nuclei have been recognized to reflect and modulate important cell behaviors such as migration and cancer cell malignant tendency. However, these nuclear properties are difficult to characterize accurately using conventional measurement methods, which are often based on probing or deforming local sites over a nuclear region. The corresponding results are sensitive to the measurement position, and they are not decoupled from the cytoplasmic properties. Microfluidics is widely recognized as a promising technique for bioassay and phenotyping. In this report, we develop a simple and nondestructive approach for the single-cell quantification of nuclear elasticity based on microfluidics by considering different deformation levels of a live cell captured along a confining microchannel. We apply two inlet pressure levels to drive the flow of human nasopharyngeal epithelial cells (NP460) and human nasopharyngeal cancerous cells (NPC43) into the microchannels. A model considering the essential intracellular components (cytoplasm and nucleus) for describing the mechanics of a cell deforming along the confining microchannel is used to back-calculate the cytoplasmic and nuclear properties. On the other hand, we also apply a widely used chemical nucleus extraction technique to examine its possible effects (e.g., reduced nuclear modulus and reduced lamin A/C expression). To determine if the decoupled nuclear properties are representative of cancer-related attributes, we classify the NP460 and NPC43 cells using the decoupled physical properties as classification factors, resulting in an accuracy of 79.1% and a cell-type specificity exceeding 74%. It should be mentioned that the cells can be recollected at the device outlet after the nondestructive measurement. Hence, the reported cell elasticity measurement can be combined with downstream genetic and biochemical assays for general cell research and cancer diagnostic applications.

 Received 17th July 2020,
Accepted 24th September 2020

DOI: 10.1039/d0lc00725k

rsc.li/loc

Introduction

Nuclear mechanical properties are widely recognized to correspond with cancer cell migration.¹ Metastasis is lethal

and has caused over 90% of cancer deaths in recent years.^{2–4} Once metastasis occurs, the cancer often becomes nearly non-eliminable and highly mortal.^{4,5} The key steps in metastasis are the intravasation of primary tumor cells^{6,7} and the extravasation of circulating tumor cells (CTCs).^{8,9} Existing studies related to whole-cell stiffness have revealed that cancerous cells are usually more deformable compared to benign cells, implying that they can migrate to other body sites and establish new colonies.^{10,11} In fact, the deformabilities of both the cell cytoplasm and nucleus influence cell metastasis, especially in the intravasation and extravasation stages. Since the gaps between either endothelial cells or epithelial cells are typically smaller than the nuclear size, the nuclei must deform largely during intravasation and extravasation, suggesting that the nuclear elasticity determines the occurrence of metastasis to a certain extent.^{12,13} Single-cell biomechanical phenotypes have been recognized for their clinical significance. For instance, cell stiffness is considered as an effective biomarker for cancers

^a Department of Biomedical Engineering, City University of Hong Kong, Hong Kong, China. E-mail: rhwlam@cityu.edu.hk; Fax: +852 3442 0172; Tel: +852 3442 8577

^b Department of Anatomical and Cellular Pathology, Chinese University of Hong Kong, Hong Kong, China. E-mail: annatsang@cuhk.edu.hk

^c BGI-Shenzhen, Shenzhen 518083, Guangdong, China

^d Guangdong High-Throughput Sequencing Research Center, Shenzhen, Guangdong, China

^e School of Biomedical Sciences, The University of Hong Kong, Hong Kong, China

^f Department of Architecture and Civil Engineering, City University of Hong Kong, Hong Kong, China

^g Department of Economics and Finance, City University of Hong Kong, Hong Kong, China

^h City University of Hong Kong Shenzhen Research Institute, Shenzhen, China

ⁱ Centre for Biosystems, Neuroscience, and Nanotechnology, City University of Hong Kong, Hong Kong, China

† Electronic supplementary information (ESI) available. See DOI: 10.1039/d0lc00725k

* These authors contributed equally to this work.

such as lung carcinoma¹⁰ and ovarian cancer.¹⁴ Therefore, the accurate characterization of the nuclear elastic properties can reflect the metastatic tendency of cancer cells.

A number of strategies have been reported for measuring nuclear stiffness. Most of these studies focused on the whole-cell region containing a nucleus^{15,16} or isolated nuclei.^{17,18} These measured nuclear regions in whole cells present remarkably higher stiffness compared to the corresponding peripheral/cytoplasmic regions.¹⁹ However, the degree to which the measured stiffness is representative of the nuclear elastic modulus is often undetermined. Further, theoretical models have been proposed for the different whole-cell measurement approaches to estimate the nuclear elasticity based on whole-cell body deformation.^{18,20,21} For instance, atomic force microscopy (AFM) indentation measurements on intact adherent cell bodies have been used to predict the nuclear stiffness by considering the subcellular structures as a combination of multiple viscoelastic elements.²² However, the predicted nuclear stiffness is sensitive to the probing position in the nuclear region. Additionally, in direct measurements of nuclear properties, isolated nuclei can be extracted using either mechanical or chemical approaches by destructing the cell cortexes and killing the cells.¹⁸ To determine the nuclear mechanical properties, AFM and micropipette aspiration can be applied to measure the isolated nuclei.^{23,24} Nevertheless, the mechanical or chemical nuclear extraction process may alter the composition of lamin in the nuclear envelope and suspension environment (*e.g.*, osmotic pressure) of the extracted nuclei, reducing the reliability of the mechanical quantification results.²² Measurement throughput can be another limitation of these methods.

On the other hand, microfluidics can achieve highly effective and promising single-cell processes and analyses, and a number of microfluidic systems have been reported over the past decade.^{25–27} Several microfluidic platforms have been developed for cell biomechanical characterization. For instance, a microprobe-assisted microfluidic elasticity cytometer has been developed for measuring the elastic modulus of flowing cells under large deformation.²⁸ Deeper theoretical analyses on cell deformation and mechanical stresses during cell–fluid interactions have provided more detailed characterizations of cell viscoelasticity.²⁹ Apart from the whole-cell level, microfluidics can achieve single-cell nuclear biomechanical characterization. For instance, researchers have developed microfluidics-assisted cell indentation¹³ and aspiration³⁰ strategies for characterizing nuclear mechanics; however, partial nuclear deformation still occurs, limiting the measurement repeatability and reliability.

In this work, we establish a microfluidic technique for the measurement of nuclear elasticity based on large whole-cell deformation, to the extent that the nucleus is also deformed. Cell deformation is achieved by placing an individual cell along a confining microchannel under continuous flow such that the cell is clamped by the narrowing sidewalls along the

microchannel. We previously developed and optimized the confining microchannels to quantify the whole-cell mechanical properties.²⁷ We also previously discovered the “modulus jump,” which refers to the significantly larger whole-cell elasticity for large cell deformation compared to that for relatively small deformation.³¹ This implies that the level of the modulus jump can reflect the nuclear elasticity. Herein, we further develop a strategy based on a representative hyperelastic Tataro model describing the cell mechanics to decouple the contributions of the cytoplasmic and nuclear elasticities for a floating cell measured under large deformation. Notably, the proposed nuclear characterization strategy can be applied directly to floating cells (*e.g.*, CTCs) as well as the dissociated and suspended adherent cells. Meanwhile, the proposed strategy is also capable of quantifying cell mechanical properties in blood samples.³² Nasopharyngeal carcinoma has been reported to have high incidence and an increasing mortality rate in the southern areas of China in recent years.^{33–35} Since nasopharyngeal tumors have been recognized to be associated with the Epstein–Barr virus (EBV), studying the EBV-positive cancer cell line NP460 can provide valuable information for nasopharyngeal cancer and EBV research.³⁶ On the other hand, nasopharyngeal epithelial cell line NP460 has been used as a comparative model to study the role of inflammatory cytokines in regulating EBV infection in premalignant nasopharyngeal epithelial cells.³⁷ The results of this work also improve our understanding of the biomechanical properties of related nasopharyngeal cancer cells. Altogether, this work demonstrates a simple and reliable approach for the quantification of nuclear biomechanical properties.

Methods

Device fabrication

The microfluidic device was fabricated mainly based on a two-step soft photolithography process in which a replica polydimethylsiloxane (PDMS) molding was used to transfer high-aspect-ratio microstructures from a silicon mold to a PDMS substrate.³⁸ The silicon mold master was manufactured by patterning a positive photoresist (AZ5214, AZ Electronic Materials, Branchburg, NJ) on a silicon wafer followed by deep reactive ion etching (DRIE) and stripping the photoresist. Next, the first-stage standard replica molding process was carried out using the silicon mold master to obtain a PDMS substrate with the reversed microstructures acting as a negative mold. A molecular layer of trichloro(1*H*,1*H*,2*H*,2*H*-perfluoro-octyl)silane (Sigma-Aldrich) was deposited on the microstructures of the PDMS mold. The silanized PDMS mold was then immersed in deionized water and placed in an oven for 1 h to remove any excess silane coating. Another round of the standard replica molding of PDMS on the silanized PDMS mold was then carried out. Holes were punched at the inlets and outlets of the PDMS substrate. The micropatterned side of the newly molded

PDMS substrate was bonded on a glass slide using oxygen plasma treatment (Plasma Prep II, SPI Supplies) to form the microfluidic device. Afterward, cell-repelling pluronics F-127 (Sigma-Aldrich) molecules were applied along the microchannels to prevent cell attachment on the microchannel walls.

Cell culture

An immortal human nasopharyngeal epithelial cell line (NP460) and a nasopharyngeal cancerous cell line (NPC43) were extracted from nasopharyngeal cancer patients and expanded in culture flasks. NP460 cells were cultured in the 50% complete Eplife medium (Thermo Fisher Scientific) and 50% complete Defined Keratinocyte-SFM (Thermo Fisher Scientific) with 100 units per ml penicillin and $100 \mu\text{g ml}^{-1}$ streptomycin. NPC43 cells were cultured in RPMI-1640 (Sigma) with 10% fetal bovine serum, $4 \mu\text{M}$ Y27632 dihydrochloride (Alexis), 100 unit per ml penicillin, and $100 \mu\text{g ml}^{-1}$ streptomycin.

Both cell types were cultivated in an incubator at 37°C under saturated humidity and 5% CO_2 in air. Once the cell population reached $\sim 80\%$ confluence, cell passaging was performed by applying 0.25% trypsin-EDTA, centrifuging, and resuspending the cells in fresh media for subsequent incubation.

Nucleus extraction

The cells were suspended in 0.25% trypsin-EDTA, transferred into a pre-chilled syringe tube, and centrifuged. The culture medium was then removed by aspiration. After the application of hypotonic buffer solution (20 mM Tris-HCl, 10 mM NaCl, and 3 mM MgCl_2) and pipetting, the cells were placed in a syringe tube in ice for 20 min. Next, 10% NP40 detergent (Thermo Fisher Scientific) was added to the cell suspension and vortex-mixed at 2500 rpm for 15 s to chemically extract the cell nuclei. The biosample was further processed through $37 \mu\text{m}$ cell strainers (STEMCELL Technologies Inc.) to remove the larger cell debris. After centrifuging and removing the supernatant, which mostly contained the cytoplasmic fraction, the remaining pellet was resuspended to obtain the nuclei.

Fluorescence staining

Hoechst 33342 (Thermo Fisher Scientific) with a concentration of $0.1 \mu\text{g ml}^{-1}$ in HBS or culture medium was applied for 5 min to stain DNA in either whole cells or extracted nuclei. Immunofluorescence staining was applied to both the suspended intact cells and the extracted nuclei. To stain the nucleoskeleton of the suspended intact cells, they were first detached by 0.25% trypsin-EDTA in phosphate-buffered saline (PBS; Sigma-Aldrich, St. Louis, MO). Each population of $\sim 10^5$ cells was transferred to a syringe tube for the following steps. The cell sample was centrifuged followed by aspiration and the addition of 4% paraformaldehyde (PFA; Sigma-Aldrich, St. Louis, MO) for 15

min to fix the cells. Next, the cells were centrifuged and aspirated, and PBS was pipetted into the cells as a cell-washing process. Triton X-100 was added to the cell culture (PBS) at a 0.3% volumetric ratio for 20 min to permeabilize the cells. The solution was then replaced with 3% bovine serum albumin (BSA) for 1 h to prevent non-specific binding in the following steps. The cells were then incubated in a primary antibody (lamin A/C monoclonal antibody; Thermo Fisher Scientific) at a dilution ratio of 1:100 in 3% BSA for 1 h followed by washing the cells with the final cell culture solution (BSA). The cells were then incubated in a secondary antibody (Alexa-555; Life Technologies, Carlsbad, CA) at a dilution ratio of 1:1500 in 3% BSA in the dark for 1 h. After washing the cells twice, they were resuspended to obtain a cell concentration of $\sim 10^5$ cells per ml. To stain the nucleoskeleton in the isolated nuclei, they were extracted using the procedures described in the preceding section, and the staining procedure was the same as for the suspended intact cells.

Cell viability test

The cell viability was tested using a LIVE/DEAD cell viability kit (Life Technologies). The prepared staining reagents were added into the cell suspensions at room temperature for 20 min to stain the live/dead cells with different fluorescent signals.

Image capture and processing

Bright-field microscopic images were captured under an inverted microscope (TE300, Nikon) equipped with an sCMOS microscope camera (Zyla 4.2, Andor). The captured microscopic images were processed using ImageJ (NIH) to obtain the key parameters (*i.e.*, the diameters of cells and nuclei as well as the penetration length in confining channels). The elastic moduli were computed using customized MATLAB scripts (2017a, MathWorks, MA, USA) written by the authors. Immunofluorescence images were captured using a confocal laser scanning microscope (ZEISS LSM 880). The fluorescence intensity in each captured confocal image was measured using ImageJ.

Simulation

The laminar flow along a cell/nucleus-containing confining microchannel was simulated in COMSOL 5.2a (Burlington, MA). The pressure distribution around a cell/nucleus with a size ranging from 6–20 μm at a defined position along the microchannel was analyzed for the case of a driving pressure of 1 kPa. Briefly, laminar flow physics was applied to compute the pressure distributions for situations where a cell/nucleus was captured in different positions of single confining microchannels. We directly built the geometries of a cell/nucleus at different positions in COMSOL 5.2a. The driving fluid was selected as water from the material library, and the captured cell/nucleus was represented as a blank material with the appropriate properties added [density =

1110 kg m⁻³ (ref. 39) and dynamic viscosity = 0.033 Pa s (ref. 40)]. A fine mesh for fluid dynamics was used in the simulations. The governing equations in the laminar flow simulation are:

$$\rho(u \cdot \nabla)u = \nabla \cdot [-p + \mu(\nabla u + (\nabla u)^T)] + F, \quad (1)$$

and

$$\rho \nabla \cdot (u) = 0, \quad (2)$$

where ρ is the density of the fluid; u is the fluid velocity; μ is the fluid dynamic viscosity; p is the fluid pressure; and F is the force contributed by the interfacial forces at the adjacent interface. The channel inlet and outlet pressures were considered to be 1 and 0 kPa, respectively, and the cell–fluid interface was considered to be the interior wall to compute the pressure distributions for each case. Next, the effective drag force on the captured cell/nucleus was calculated by integrating the surface stresses in the flow direction on the captured cell/nucleus surface using the ‘Surface Integration’ function in COMSOL 5.2a.

Classification regime

Cell classification was based on the quadratic discriminate analysis (QDA) regime. The classification of cell lines was determined according to two cell/nucleus property variables in QDA. We created customized scripts to classify the scatters of the two cell variables and elasticity using MATLAB R2017a (MathWorks).

Statistics

All error bars in plots represent standard errors. Student's *t*-test was used to calculate *p*-values.

Results and discussion

Design of the confining microchannel

The microfluidic device (Fig. 1a), which includes two arrays of confining microchannels with 40 microchannels in each array, can be used to quantify the physical properties of floating cells and soft spherical particles, as reported in our previous studies.²⁷ The prepared samples can be driven into the microfluidic device by pressure-adjustable compressed air flow, and the compressed air flow pressure can be reduced and regulated using a pressure-reducing regulator. Because the flow resistance will be dramatically increased after a cell/nucleus is captured in a single microchannel, the following floating cells are expected to be captured in other ‘blank’ microchannels. In the ideal case, approximately 80 cells/nuclei are captured for a single experiment. In this work, we nondestructively quantified the nuclear elasticity of NP460 and NPC43 cells by capturing the whole cells in the confining microchannels. For comparison, we also captured the chemically extracted nuclei and measured their elasticity.

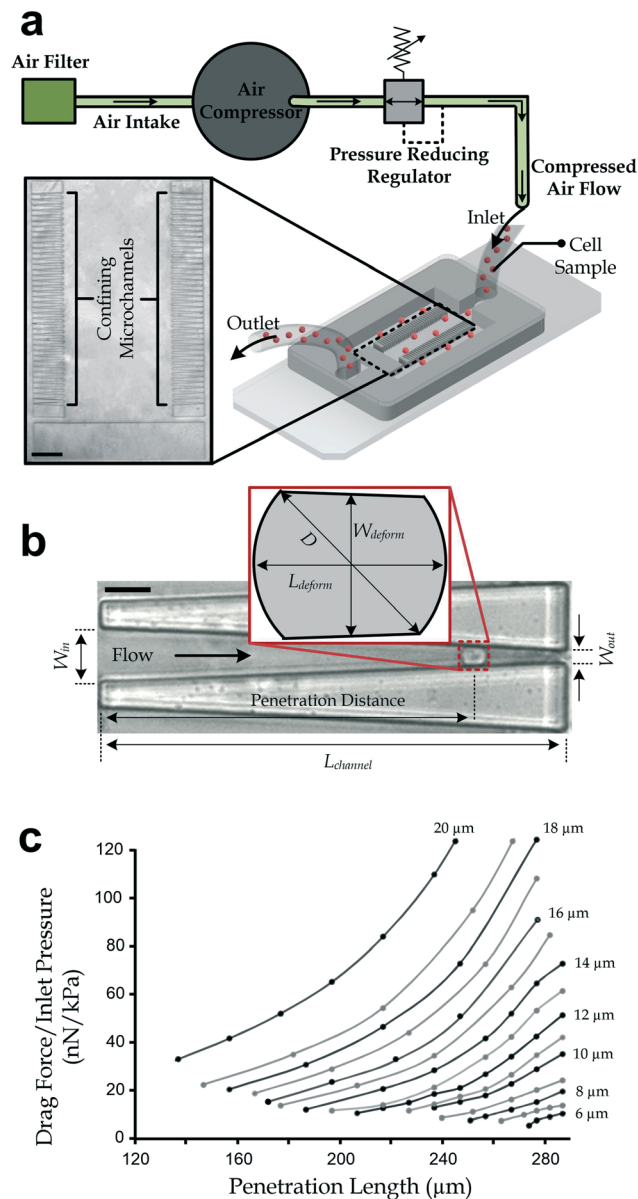


Fig. 1 (a) Basic structure of the microfluidic device and the pressure driving configurations. Inset: Arrays of confining microchannels. Scale bar: 300 μm . (b) Representative microscopic image of a deformed cell captured in a confining channel. Scale bar: 20 μm . Inset: Key parameters of a deformed cell. (c) Calculated drag force values against the penetration lengths of cells with different nuclear diameters.

Each confining microchannel is configured as a linear confined shape, the width of which decreases from W_{in} at its inlet to W_{out} at its outlet. W_{in} should be large enough to cover the size range of the whole cells, whereas W_{out} should be small enough to capture the extracted cell nuclei of both NP460 and NPC43 cells. Driven by a constant hydraulic pressure from the channel entrance, a cell or nucleus captured along the channel must deform because of the direct contact with the channel side walls, with their separation distance reducing during the flow, as shown in Fig. 1b. Here, we define the confining angle θ (illustrated in

the inset of Fig. 1b) to reflect the rate of change of the channel width along the channel length. The value of θ should be small enough to approximate the shape of the captured particle as a sphere with its top and bottom chopped off. We set the channel length L_{channel} to be sufficiently large to guarantee a small θ with the relation $\theta = \tan^{-1}((W_{\text{in}} - W_{\text{out}})/(2L_{\text{channel}}))$. Further, we express the particle position as the distance from the microchannel inlet and call it the “penetration length.”

Considering that the dimensions of a microchannel are largely dependent on the sizes of the target particles, we measured the diameters of the whole cells and nuclei of both the NP460 and NPC43 cells (to our understanding, these values have not yet been reported). The measurement of the whole cells was straightforward – we suspended the cells by trypsinization and quantified their diameters under a bright-field microscope. We obtained diameters of $13.84 \pm \text{SD } 1.99 \mu\text{m}$ ($N = 90$) for NP460 cells and $14.18 \pm \text{SD } 2.54 \mu\text{m}$ ($N = 103$) for NPC43 cells. On the other hand, we applied fluorescence staining with Hoechst 33342 to visualize the nuclei in the whole cells or chemically extracted nuclei (the procedures for nucleus extraction are available in Methods). We measured the diameters of these nuclei of both cell types as shown in Fig. 2a. Notably, the suspended cells and nuclei typically had spherical shapes. Moreover, we observed the three-dimensional (3D) shapes of the Hoechst 33342-stained nuclei of both NPC43 and NP460 cells using laser confocal microscopy to further verify the 3D

nuclear shapes (see Fig. S1 in ESI†). Generally, NPC43 cells presented a larger nuclear diameter (unextracted: $11.18 \pm \text{SD } 1.62 \mu\text{m}$, $N = 40$; chemically extracted: $11.27 \pm \text{SD } 1.75 \mu\text{m}$, $N = 40$) comparing to the NP460 cells (unextracted: $9.86 \pm \text{SD } 1.55 \mu\text{m}$, $N = 40$; chemically extracted: $10.18 \pm \text{SD } 1.29 \mu\text{m}$, $N = 40$), as summarized in Fig. 2b. Based on these measured whole-cell and nuclear sizes, we configured the dimensions of the confining microchannels as $W_{\text{in}} = 30 \mu\text{m}$, $W_{\text{out}} = 4 \mu\text{m}$, and $L_{\text{channel}} = 300 \mu\text{m}$ such that $\theta \approx 2.5^\circ$. Additionally, the channel height was set as $50 \mu\text{m}$ to avoid unwanted physical contact between the captured cells/nuclei and the microchannel roof and floor. This channel height was regulated by adopting the corresponding processing time during device fabrication *via* DRIE.

In our previous research, we adopted Hertz's and Tataru's theories⁴¹ to calculate the whole-cell elasticity based on the cell deformation along a confining microchannel.²⁷ Likewise, this approach can be applied to calculate the nuclear elasticity considering that cell nuclei generally behave as homogeneous soft spheres.^{42–45} The flow along the confining microchannel is laminar with a very small Reynolds number ($\ll 1$) given the micro-scale channel dimensions.⁴⁶ We simulated the drag force over a deformed cell/nucleus with a defined diameter along a confining microchannel at different penetration lengths under a driving pressure of 1 kPa (see Methods for detailed procedures). For each case, we obtained a drag force for a certain cell/nucleus diameter and a certain penetration length, as summarized in Fig. 1c. It should be mentioned that the drag force scales linearly with the driving pressure because of the laminar flow characteristics. Therefore, under a steady driving pressure, we can convert the penetration length L and particle diameter D to the drag force over the captured particle based on the numerical interpolation using adjacent pre-computed values, as indicated in Fig. 1c. The value of L , which can be directly observed under a microscope, determines the deformed particle length W_{deform} along the channel width direction with the relation $W_{\text{deform}} = (W_{\text{out}} - W_{\text{in}})L_{\text{channel}}/L + W_{\text{in}}$. The value of D can be calculated based on the assumption that the volume of the deformed particle does not change:

$$D = \sqrt[3]{\frac{3L_{\text{deform}}^2 W_{\text{deform}} - W_{\text{deform}}^3}{2}} \quad \text{or} \quad L_{\text{deform}} = \sqrt{\frac{2D^3}{3W_{\text{deform}}} + \frac{W_{\text{deform}}^2}{3}}, \quad (3)$$

where L_{deform} is the particle length along the channel length direction. The equivalent elastic modulus E can then be obtained by considering the force-balanced state of the captured particle and the hyperelastic Tataru model:⁴⁷

$$E = \left[\frac{3}{4} \left(\frac{2}{D_c} + \frac{\Theta D_c}{L_{\text{deform}}^2} \right) - \frac{8D^2 + D_c^2}{\pi(8D^2 + 2D_c^2)^{3/2}} \left(1 + \frac{\Theta D_c^2}{5L_{\text{deform}}^2} \right) \right] \frac{3\Phi F_{\text{drag}}}{4(D - W_{\text{deform}}) \sin \theta}, \quad (4)$$

where F_{drag} is the drag force on the particle, $D_c (= (D^2 - W_{\text{deform}}^2)^{1/2} - D - L_{\text{deform}})$ is the diameter of the contact area between the cell body and each side of the microchannel walls, and Φ and Θ are the correction factors as functions of

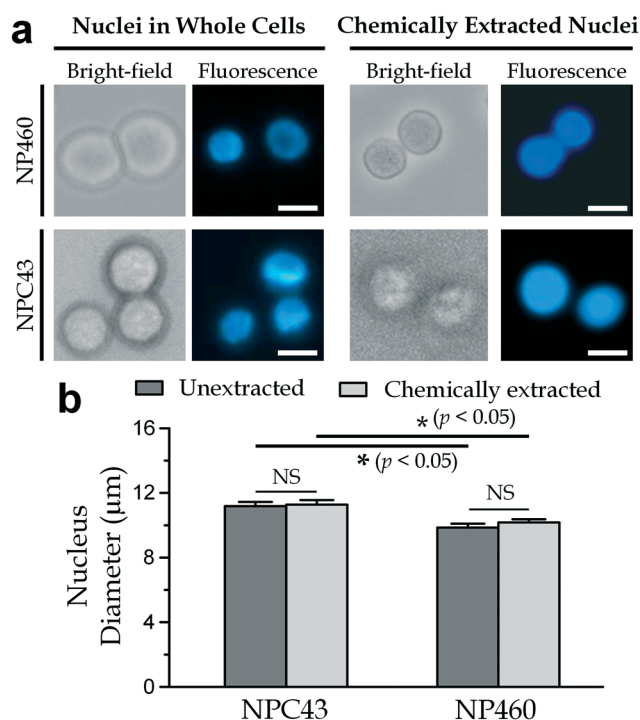


Fig. 2 (a) Bright-field and fluorescence micrographs of the whole cells (left) and chemically extracted nuclei (right) of suspended NP460 and NPC43 cells. The fluorescence images show the stained cell nuclei. Scale bar: $10 \mu\text{m}$. (b) Nuclear diameters of the whole cells and extracted nuclei of NPC43 and NP460 cells ($N = 40$ for both cell types). Error bars are the standard errors of the mean. Asterisk indicates $p < 0.05$. NS indicates $p \geq 0.05$.

the deformation level $\xi (= 1 - W_{\text{deform}}/D)$ for the hyperelastic properties, which are respectively calculated by

$$\Phi = \frac{(1-\xi)^2}{1-\xi + \xi^2/3} \quad \text{and} \quad \Theta = \frac{1-\xi/3}{1-\xi + \xi^2/3}. \quad (5)$$

Nondestructive measurement of nuclear elasticity

As discussed previously, nondestructive measurements of a nucleus in an intact cell retain cell viability as well as the material properties of the nucleus. Here, we adopt the microfluidic confining channel to quantify both the cytoplasmic elasticity and nuclear elasticity of floating single cells, including the dissociated adherent epithelial cells.^{27,32}

According to our previous study on human breast cells, the measured whole-cell elasticity is significantly higher under high driving pressure (>300 Pa) compared to under lower driving pressure (~ 100 Pa); we call this increase the “modulus jump”.³¹ Since the pressure distributed in the confining channels dominates over 99% of the pressure difference between the device inlet and outlet (see Fig. S2 in ESI† for details), we can directly use the driving pressures applied to the microfluidic device as the pressure differences between the confining channel entrances and exits in the calculations. In this work, we first measured the elasticity values of NP460 and NPC43 cells under two pressure levels (100 and 400 Pa) using a confining microchannel. Sample microscopic images of deformed NP460 and NPC43 cells with their nuclei stained with Hoechst 33342 under the two pressure levels are illustrated in Fig. 3a and b. The measured results were then converted to the whole-cell elasticity using eqn (3)–(5) (Fig. 3c), revealing the modulus jumps for both NP460 and NPC43 cells.

To resolve the cytoplasmic and nuclear elasticity values, we adopt a simplified physical cell structure consisting of only the cytoplasm and nucleus⁴⁸ to represent the key biomechanical properties of a captured cell. The measured cell deformation can then be considered as the nucleus and the cytoplasmic body being compressed simultaneously inside the confining microchannel, as presented in Fig. 3d. Considering that the elasticity of the nucleus is often higher than that of the cytoplasmic body in a cell,⁴⁹ the modulus jumps should correspond to the presence of nuclear deformation by the confining microchannel sidewalls, as we have previously reported.³¹

According to the force balance as described in Fig. 3d, the compressive force should have the following relation with drag force: $F_{\text{drag}} = 2F_{\text{compress}}/\sin\theta$. F_{compress} can be calculated by multiplying the driving pressure P with the normalized compressive force at 1 kPa, denoted as F^* , as described previously in Fig. 1c. Because the penetration length L can be converted to W_{deform} , F^* is a function of D and W_{deform} . Hence, eqn (4) can be rewritten as

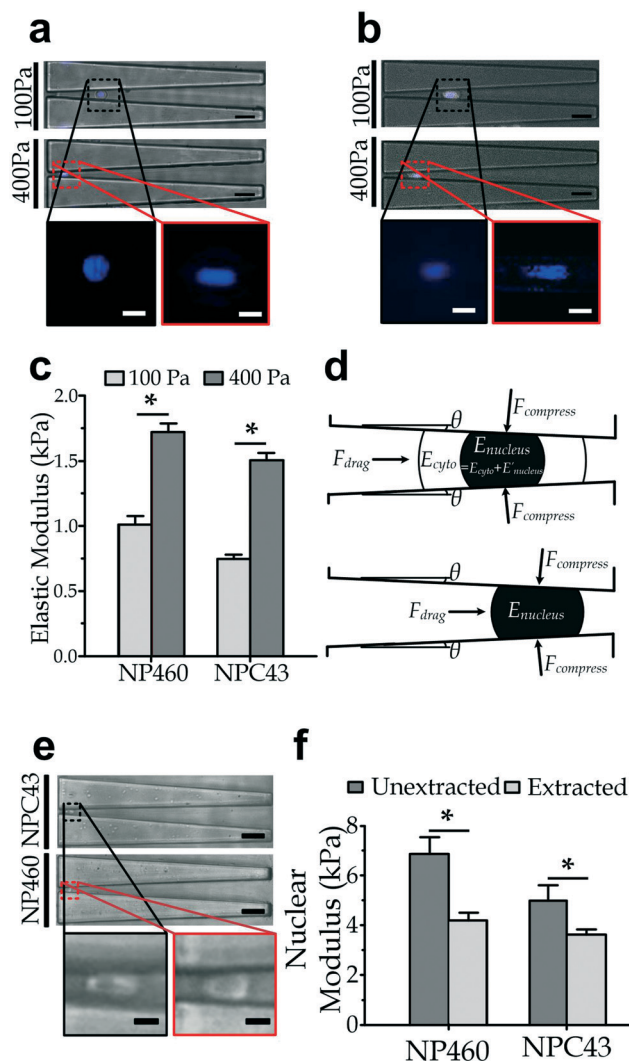


Fig. 3 (a) An NP460 cell and (b) an NPC43 cell captured in a microchannel under 100 and 400 Pa. Scale bar: 30 μm . Inset: Enlarged fluorescent images of the nuclear part under the two pressures. Scale bar: 10 μm . (c) Elastic moduli of NPC43 and NP460 cells under the two driving pressures, asterisk indicates $p < 0.05$. (d) Diagram of key parameters in a largely deformed whole cell (top) and in a deformed extracted nucleus (bottom). E_{cyto} represents the elastic modulus of the cytoplasm, and E_{nucleus} represents the elastic modulus of the nucleus, which has a modulus level E'_{nucleus} larger than E_{cyto} . (e) Representative images of an extracted nucleus captured in a microchannel. Scale bar: 30 μm . Inset: Enlarged nuclear deformations in a microchannel. Scale bar: 5 μm . (f) Nuclear moduli of the chemically extracted nuclei ($N = 30$ for NP460 cells and $N = 40$ for NPC43 cells) and those measured using the nondestructive method for whole cells with unextracted nuclei ($N = 48$ for NPC43 cells and $N = 47$ for NP460 cells). Error bars are the standard errors of the mean. Asterisk indicates $p < 0.05$.

$$F_{\text{compress}} = P \times F^*(D, W_{\text{deform}}) = K(D, W_{\text{deform}}) \times E(D, W_{\text{deform}}), \quad (6)$$

where K is a function of D and W_{deform} . Furthermore, we define the cytoplasmic modulus as E_{cyto} and the nuclear modulus as E_{nucleus} . We further define E'_{nucleus} as the level of the nuclear modulus higher than E_{cyto} ; therefore, $E_{\text{nucleus}} =$

$E_{\text{cyto}} + E'_{\text{nucleus}}$. Clearly, the compressive force driven by the inlet pressure is distributed into two smaller compressive forces for the nucleus and the cytoplasmic body. Therefore, considering that the compressive forces F_1 and F_2 are respectively caused by the driving pressures of $P_1 = 100$ Pa and $P_2 = 400$ Pa, we have the following approximations:

$$F_1 = P_1 \times F^*(D_{\text{cell}}, W_1) \approx K(D_{\text{cell}}, W_1)E_{\text{cyto}} + K(D_{\text{nucleus}}, W_1)E'_{\text{nucleus}}, \quad (7)$$

and

$$F_2 = P_2 \times F^*(D_{\text{cell}}, W_2) \approx K(D_{\text{cell}}, W_2)E_{\text{cyto}} + K(D_{\text{nucleus}}, W_2)E'_{\text{nucleus}}, \quad (8)$$

where W_1 and W_2 are the deformed particle widths at driving pressures P_1 and P_2 , respectively. It should be mentioned that calculation of above two K functions in eqn (7) and eqn (8) is straightforward. Considering the relation described in eqn (6), we can obtain the cytoplasmic K value as $F_1/E(P_1, D_{\text{cell}}, W_1)$ and the other K value as $F_1/E(P_1, D_{\text{nucleus}}, W_1)$ in eqn (7). We also obtain the two K values in eqn (8) in the same way. Apparently, E_{cyto} and E_{nucleus} can be computed by solving

$$\begin{bmatrix} E_{\text{cyto}} \\ E_{\text{nucleus}} - E_{\text{cyto}} \end{bmatrix} \approx \begin{bmatrix} K(D_{\text{cell}}, W_1) & K(D_{\text{nucleus}}, W_1) \\ K(D_{\text{cell}}, W_2) & K(D_{\text{nucleus}}, W_2) \end{bmatrix}^{-1} \begin{bmatrix} P_1 F^*(D_{\text{cell}}, W_1) \\ P_2 F^*(D_{\text{cell}}, W_2) \end{bmatrix}. \quad (9)$$

Quantification of nuclear elasticity

We nondestructively quantified the nuclear moduli of NP460 and NPC43 cells using the confining microchannels. The cell nuclei were visualized by fluorescent pre-staining. The cell density was then diluted to a sufficiently low level (10^4 nuclei per mL) to avoid cell aggregation along the microchannels. We injected the cells into the microfluidic device with a driving pressure of 100 Pa and then collected microscopic images of the captured cells to obtain F_1 , W_1 , D_{cell} , and D_{nucleus} for every cell. Next, we increased the driving pressure to 400 Pa and again collected microscopic images to obtain F_2 and W_2 . Afterward, we increased the driving pressure to 1 kPa to recollect all the captured cells at the device outlet for further analysis. The following E_{cyto} and E_{nucleus} values were then obtained using eqn (7)–(9), as shown in Fig. 3f: $E_{\text{cyto}} = 0.72 \pm \text{SE } 0.03$ kPa and $E_{\text{nucleus}} = 4.99 \pm \text{SE } 0.62$ kPa for NPC43 cells ($N = 48$) and $E_{\text{cyto}} = 0.89 \pm \text{SE } 0.05$ kPa and $E_{\text{nucleus}} = 6.87 \pm \text{SE } 0.68$ kPa for NP460 cells ($N = 47$). The quantified elastic moduli of the non-extracted nuclei using our model are within the same order of magnitude compared to other previously reported values measured using intact cells.^{13,17}

Many works have quantified the mechanical properties of the extracted nuclei as representative properties of the nuclei in live cells.^{17,18,45,50} However, the nucleus extraction procedures, cell viability, and surrounding conditions may alter the nuclear properties. For comparison, we quantified the elasticity of the chemically extracted nuclei of NP460 and

NPC43 cells using the confining microchannels. The experimental procedures were the same as in the nondestructive measurement except that only one stage of driving pressure was applied. Because the extracted nuclei are smaller than whole cells, we set the applied pressure to deform the extracted nuclei as 300 Pa, lower than the previously used 400 Pa (Fig. 3e). The nuclear moduli were then calculated directly using eqn (4), giving values of $4.25 \pm \text{SE } 0.31$ kPa ($N = 30$) for NP460 cells and $3.34 \pm \text{SE } 0.15$ kPa ($N = 40$) for NPC43 cells. By comparing these values with the corresponding results for non-extracted cells (Fig. 3f), we observed that the extracted nuclei generally had smaller moduli than those maintained in the whole cells. This difference suggests a possible variation in nuclear properties caused by the chemical nucleus extraction process. To examine cell viability after the quantification of nuclear elasticity, we implemented cell live/dead assay on the recollected cells and the cells right before injection into the microfluidic device. The results are summarized in Fig. 4, showing that the measurement did not cause any significant increase in the portion of dead cells.

Further, we examined possible causes of the reduced moduli of the extracted nuclei by immunofluorescence staining (see Methods) for the expression of nuclear lamin A/C, which is known to contribute to nuclear deformability⁵¹ and is directly related to nuclear elasticity.⁵² To facilitate

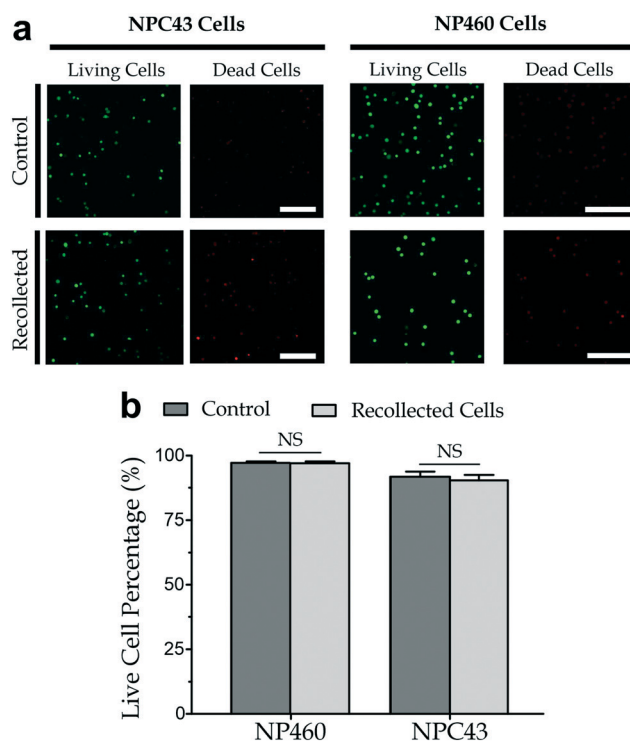


Fig. 4 (a) Viability of the cells recollected from the microfluidic device after measurement (labeled as 'Recollected') and cells before measurement (labeled as 'Control'). Scale bar: 200 μm . (b) Percentages of live cells obtained from at least 10 repeated experiments. Error bars are the standard errors of the mean. NS indicates $p \geq 0.05$ from the Student's t -test.

comparison among the staining images, we generally controlled the parameters (*e.g.*, cell density before staining, and incident laser intensity in imaging) used in immunofluorescence staining and confocal microscopy imaging. The stained fluorescence intensities for different cases were quantified based on the captured microscopic images (Fig. 5a). The results (Fig. 5b) show that the extracted nuclei had significantly lower lamin A/C expressions, suggesting the nuclear extraction process may reduce the nuclear membrane integrity and the corresponding stiffness. The lamin A/C expression for the nuclei of NPC43 ($1.36 \times 10^5 \pm \text{SE } 0.22 \times 10^5$ A.U.) was lower than that for the nuclei of NP460 ($1.89 \times 10^5 \pm \text{SE } 0.26 \times 10^5$ A.U.), in agreement with the measured nuclear moduli. Therefore, nondestructive methods should be preferred for measuring the nuclear properties.

Cell classification

We classified the NPC43 and NP460 cells based on the different measured physical properties. QDA has been

suggested to be suitable to discriminate between medical conditions that are symptomatically very similar, such as alcoholic and non-alcoholic liver disease.⁵³ In particular, QDA was reported to be effective for decimation situations in which the ratio of sample number to the number of variables is large.⁵⁴ We proposed to use two variables for classification, while the sample size is typically several dozens; thus, the ratio of sample size to number of variables was relatively large, and QDA is expected to be effective for classification. The cell-type classifications using the measured whole-cell elasticity and cell diameter under a driving pressure of 100 Pa for the ‘small’ cell deformations are provided in Fig. 6a (left). The boundary line was computed based on QDA as an optimized separating curve between the clusters of properties of the two cell types. To quantify the classification performance, we considered the accuracy (*A*), sensitivity values for NP460 (S-NP) and NPC43 (S-NPC), and the overall cell-type sensitivity (*S*), which is defined as the lower value of S-NP and S-NPC. For the case of small deformation, these values were *A* = 63.2%, S-NP = 78.3%, and *S* = S-NPC = 58.3%. We repeated the cell classification for the driving pressure of 400 Pa for the ‘large’ deformations [Fig. 6a (right)] with the classification parameters *A* = 60.6%, *S* = S-NP = 57.9%, and S-NPC = 64.8%; no improvements were obtained compared to the driving pressure of 100 Pa.

Next, we implemented QDA for cytoplasmic elasticity against cell diameter and nuclear elasticity against nuclear diameter, as presented in Fig. 6b. The classification parameters for the cytoplasmic properties were *A* = 63.0%, S-NP = 68.8% and *S* = S-NPC = 60.0%; those for the nuclear properties were *A* = 79.1%, *S* = S-NP = 74.0%, and S-NPC = 86.4%. These results suggest that the classification accuracy using the elasticity values related to cell nuclei (*A* = 79.1%) is generally higher than that obtained by directly using the whole-cell elasticity under a driving pressure (*A* < 65%); thus, the nuclear elasticity values are the more relevant cell properties. To further confirm the distinct differences in nuclear elasticity between the two cell lines, we measured and compared their distributions of nuclear diameter and nuclear elasticity (see Fig. S3 in ESI†). The results suggest that the difference in nuclear elasticity is a significant factor in classification.

As mentioned earlier, the nondestructive cell elasticity measurement and classification approach can be applied to other cell types in suspension, including both non-adherent cells and dissociated adherent cells. Further applications include the characterization and classification of other cancer cell types. Many studies have revealed alterations in the whole-cell and nuclear biomechanical properties in many other cancer types. For instance, the nuclear elasticity mainly determines cell translocations in narrow regions for breast cells.¹³ The difference in nuclear elastic moduli between the non-cancerous breast cell line (MCF-10A) and breast cancer cell line (MDA-MB-231) is more distinct than the difference between their whole-cell elastic moduli.^{50,55}

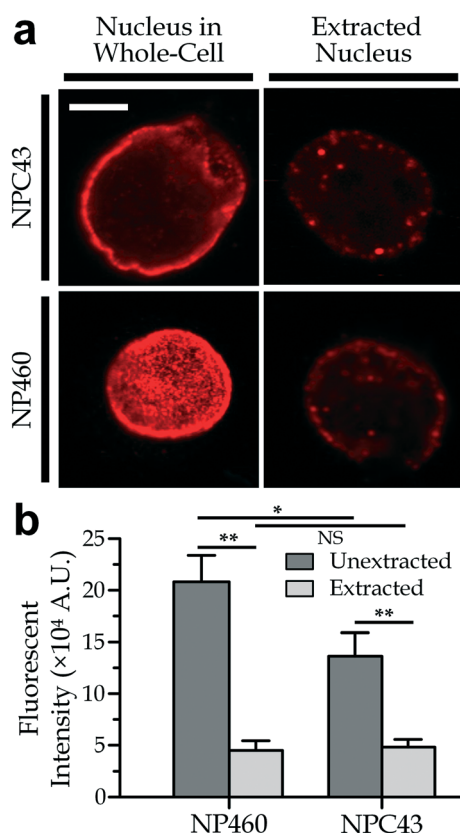


Fig. 5 (a) Immunofluorescence images of lamin A/C expression for nuclei in suspended NPC43 and NP460 cells and the chemically extracted nuclei. Scale bar: 5 μm . (b) Total fluorescence intensity of the unextracted and extracted nuclei ($N = 24$ for unextracted NPC43 nuclei, $N = 19$ for extracted NPC43 nuclei, $N = 16$ for unextracted NP460 nuclei, and $N = 21$ for extracted NP460 nuclei). Double asterisk indicates $p < 0.01$. Asterisk indicates $0.01 \leq p < 0.05$. NS indicates $p \geq 0.05$.

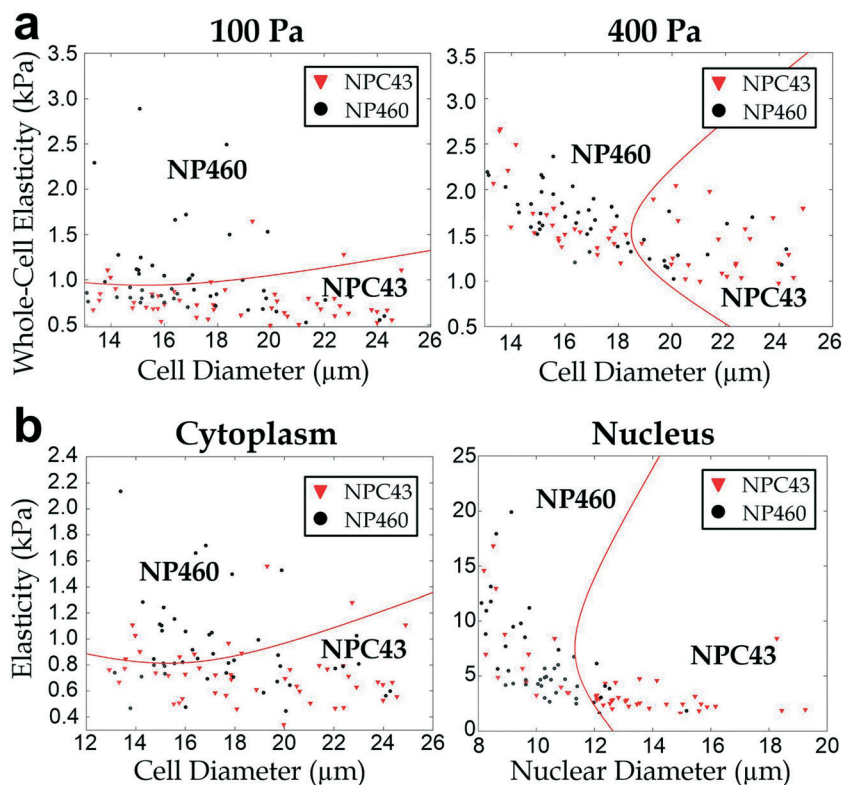


Fig. 6 (a) Cell classification based on whole-cell elastic moduli under 100 Pa (left) and 400 Pa (right) against cell diameter. $N \geq 47$ for either cell type. (b) Cell classification based on cytoplasmic elasticity versus cell diameter (left) and nuclear elasticity versus nuclear diameter (right).

Conclusions

In this work, we successfully established a nondestructive cell quantification strategy for revealing the nuclear and cytoplasmic elasticity levels of floating cells, including both non-adherent cells and dissociated adherent cells. Based on hyperelastic Tataru theory, we derived a model that considers a cell with a nucleus inside its cytoplasm for converting multiple cell deformation levels of a cell trapped along a confining microchannel to the nuclear and cytoplasmic elastic moduli. We further applied the nondestructive measurement to quantify the elasticities of non-cancerous (NP460) and cancerous (NPC43) human nasopharyngeal cells, revealing that NPC43 cells have softer nuclei ($4.99 \pm \text{SE } 0.62$ kPa) than NP460 cells ($6.87 \pm \text{SE } 0.31$ kPa). Notably, the proposed nondestructive method has minimal effects on the nuclear properties compared to other destructive methods such as chemical nuclear extraction. We found that the chemically extracted nuclei exhibited reduced elastic moduli, likely caused by the removal of surface molecules including lamin A/C over cell nuclei. In contrast, our nondestructive method did not result in such alterations to the nuclear surface.

Cell classification was also performed using the NP460 and NPC43 cells. The results demonstrated that the nuclear elasticity is more representative (79.1% accuracy and 74% overall cell-type specificity) than the whole-cell elasticity ($\leq 63.2\%$ accuracy and $\leq 58.3\%$ overall cell-type specificity) for distinguishing between normal and cancer nasopharyngeal

cells. Considering that whole-cell stiffness is recognized as a good identifier of cancer cells, the nuclear elasticity measured by our nondestructive method can be further applied to cancer identification and diagnosis. Importantly, the reported method is also feasible for downstream genetic or biochemical cell characterizations because the cells can be recollected after measurement. Such integrated consideration of the genetic, biomechanical, and biochemical properties allows a deeper phenotyping of floating cells. Altogether, this work provides a nondestructive technique for the measurement of cell elasticity that is highly compatible with existing cell assays. The proposed method is promising for the comprehensive and deep phenotyping of cells for a broad range of biomedical applications, including cell research and cancer diagnosis.

Conflicts of interest

We plan to apply a US patent with the nuclear measurement scheme *via* the Knowledge Transfer Office of City University of Hong Kong with the application number PWG/PA/878/7/2020 (US pro) and the inventors Raymond H. W. Lam and Jifeng Ren. There are no other conflicts to declare.

Acknowledgements

We acknowledge financial support from the National Natural Science Foundation of China (NSFC 31770920), General Research Grant (Project No. 11204317), and Collaborative

Research Fund (Project No. C1013-15GF) of the Hong Kong Research Grant Council.

References

- 1 Y. Fu, L. K. Chin, T. Bourouina, A. Q. Liu and A. M. VanDongen, *Lab Chip*, 2012, **12**, 3774–3778.
- 2 X. Guan, *Acta Pharm. Sin. B*, 2015, **5**, 402–418.
- 3 G. P. Gupta and J. Massagué, *Cell*, 2006, **127**, 679–695.
- 4 A. W. Lambert, D. R. Pattabiraman and R. A. Weinberg, *Cell*, 2017, **168**, 670–691.
- 5 A. M. Alizadeh, S. Shiri and S. Farsinejad, *Tumor Biol.*, 2014, **35**, 8483–8523.
- 6 I. Ramis-Conde, M. A. Chaplain, A. R. Anderson and D. Drasdo, *Phys. Biol.*, 2009, **6**, 016008.
- 7 J. Kim, W. Yu, K. Kovalski and L. Ossowski, *Cell*, 1998, **94**, 353–362.
- 8 J. M. Barnes and M. D. Henry, in *Signaling Pathways and Molecular Mediators in Metastasis*, Springer, Dordrecht, 2011, pp. 197–219.
- 9 H. Liu, X. Zhang, J. Li, B. Sun, H. Qian and Z. Yin, *J. Cancer Res. Clin. Oncol.*, 2015, **141**, 189–201.
- 10 S. E. Cross, Y. S. Jin, J. Rao and J. K. Gimzewski, *Nat. Nanotechnol.*, 2007, **2**, 780.
- 11 S. E. Cross, Y. S. Jin, J. Tondre, R. Wong, J. Rao and J. K. Gimzewski, *Nanotechnology*, 2008, **19**, 384003.
- 12 Y. Wallez and P. Huber, *Biochim. Biophys. Acta, Biomembr.*, 2008, **1778**, 794–809.
- 13 Y. Xia, Y. Wan, S. Hao, M. Nisic, R. A. Harouaka, Y. Chen, X. Zou and S. Y. Zheng, *Small*, 2018, **14**, 1802899.
- 14 R. D. González-Cruz, J. S. Sadick, V. C. Fonseca and E. M. Darling, *Cell. Mol. Bioeng.*, 2018, **11**, 131–142.
- 15 G. Zhang, N. Fan, X. Lv, Y. Liu, J. Guo, L. Yang, B. Peng and H. Jiang, *Micromachines*, 2017, **8**, 89.
- 16 S. P. Arnoczky, M. Lavagnino, J. H. Whallon and A. Hoonjan, *J. Orthop. Res.*, 2002, **20**, 29–35.
- 17 H. Liu, J. Wen, Y. Xiao, J. Liu, S. Hopyan, M. Radisic, C. Simmons and Y. Sun, *ACS Nano*, 2014, **8**, 3821–3828.
- 18 F. Guilak, J. R. Tedrow and R. Burgkart, *Biochem. Biophys. Res. Commun.*, 2000, **269**, 781–786.
- 19 G. Coceano, M. S. Yousafzai, W. Ma, F. Ndoye, L. Venturelli, I. Hussain, S. Bonin, J. Niemela, G. Scoles, D. Cojoc and E. Ferrari, *Nanotechnology*, 2015, **27**, 065102.
- 20 A. Geltmeier, B. Rinner, D. Bade, K. Meditz, R. Witt, U. Bicker, C. Bludszweit-Philipp and P. Maier, *PLoS One*, 2015, **10**, e0134999.
- 21 Y. Kim, M. Kim, J. H. Shin and J. Kim, *Med. Biol. Eng. Comput.*, 2011, **49**, 453–462.
- 22 X. Wang, H. Liu, M. Zhu, C. Cao, Z. Xu, Y. Tsatskis, K. Lau, C. Kuok, T. Filleter, H. McNeill, C. A. Simmons, S. Hopyan and Y. Sun, *J. Cell Sci.*, 2018, **131**, jcs209627.
- 23 B. Zhang, Q. Luo, Z. Chen, Y. Shi, Y. Ju, L. Yang and G. Song, *Sci. Rep.*, 2016, **6**, 18809.
- 24 K. N. Dahl, A. J. Engler, J. D. Pajeroski and D. E. Discher, *Biophys. J.*, 2005, **89**, 2855–2864.
- 25 D. R. Gossett, T. K. Henry, S. A. Lee, Y. Ying, A. G. Lindgren, O. O. Yang, J. Rao, A. T. Clark and D. Di Carlo, *Proc. Natl. Acad. Sci. U. S. A.*, 2012, **109**, 7630–7635.
- 26 F. J. Byfield, R. K. Reen, T. P. Shentu, I. Levitan and K. J. Gooch, *J. Biomech.*, 2009, **42**, 1114–1119.
- 27 S. Hu, G. Liu, W. Chen, X. Li, W. Lu, R. H. Lam and J. Fu, *Small*, 2016, **12**, 2300–2311.
- 28 H. Sugiura, S. Sakuma, M. Kaneko and F. Arai, *IEEE Robot. Autom. Lett.*, 2017, **2**, 2002–2007.
- 29 L. Guillou, J. B. Dahl, J. M. G. Lin, A. I. Barakat, J. Husson, S. J. Muller and S. Kumar, *Biophys. J.*, 2016, **111**, 2039–2050.
- 30 P. M. Davidson, G. R. Fedorchak, S. Mondésert-Deveraux, E. S. Bell, P. Isermann, D. Aubry, R. Allena and J. Lammerding, *Lab Chip*, 2019, **19**, 3652–3663.
- 31 S. Hu, R. Wang, C. M. Tsang, S. W. Tsao, D. Sun and R. H. Lam, *RSC Adv.*, 2018, **8**, 1030–1038.
- 32 J. Ren, J. Li, Y. Li, P. Xiao, Y. Liu, C. M. Tsang, S. W. Tsao, D. Lau, K. W. Y. Chan and R. H. Lam, *ACS Biomater. Sci. Eng.*, 2019, **5**, 3889–3898.
- 33 S.-M. Cao, M. J. Simons and C.-N. Qian, *Chin. J. Cancer*, 2011, **30**, 114.
- 34 W. Chen, K. Sun, R. Zheng, H. Zeng, S. Zhang, C. Xia, Z. Yang, H. Li, X. Zou and J. He, *Chin. J. Cancer Res.*, 2018, **30**, 1.
- 35 W. Chen, R. Zheng, P. D. Baade, S. Zhang, H. Zeng, F. Bray, A. Jemal, X. Q. Yu and J. He, *Ca-Cancer J. Clin.*, 2016, **66**, 115–132.
- 36 W. Lin, Y. L. Yip, L. Jia, W. Deng, H. Zheng, W. Dai, J. Ko, K. W. Lo, G. T. Y. Chung, K. Y. Yip, S. D. Lee, J. S. H. Kwan, J. Zhang, T. Liu, J. Y. W. Chan, D. L. W. Kwong, V. H. F. Lee, J. M. Nicholls, P. Busson, X. Liu, A. K. S. Chiang, K. F. Hui, H. Kwok, S. T. Cheung, Y. C. Cheung, C. K. Chan, B. Li, A. L. M. Cheung, P. M. Hau, Y. Zhou, C. M. Tsang, J. Middeldorp, H. Chen, M. L. Lung and S. W. Tsao, *Nat. Commun.*, 2018, **9**, 1–17.
- 37 C. M. Tsang, G. Zhang, E. Seto, K. Takada, W. Deng, Y. L. Yip, C. Man, P. M. Hau, H. Chen, Y. Cao, K. W. Lo, J. M. Middeldorp, A. L. M. Cheung and S. W. Tsao, *Int. J. Cancer*, 2010, **127**, 1570–1583.
- 38 S. Wang, D. Feng, C. Hu and P. Rezai, *J. Semicond.*, 2018, **39**, 086001.
- 39 W. H. Grover, A. K. Bryan, M. Diez-Silva, S. Suresh, J. M. Higgins and S. R. Manalis, *Proc. Natl. Acad. Sci. U. S. A.*, 2011, **108**, 10992–10996.
- 40 T. Kalwarczyk, N. Ziebac, A. Bielejewska, E. Zaboklicka, K. Koynov, J. Szymanski, A. Wilk, A. Patkowski, J. Gapiński, H. J. Butt and R. Holyst, *Nano Lett.*, 2011, **11**, 2157–2163.
- 41 Y. L. Lin, D. M. Wang, W. M. Lu, Y. S. Lin and K. L. Tung, *Chem. Eng. Sci.*, 2008, **63**, 195–203.
- 42 P. Hozák, A. M. Sasseville, Y. Raymond and P. R. Cook, *J. Cell Sci.*, 1995, **108**, 635–644.
- 43 T. Harada, J. Swift, J. Irianto, J. W. Shin, K. R. Spinler, A. Athirasala, R. Diegmiller, P. C. D. P. Dingal, I. L. Ivanovska and D. E. Discher, *J. Cell. Biol.*, 2014, **204**, 669–682.
- 44 M. M. Knight, J. Van de Breevaart Bravenboer, D. A. Lee, G. J. V. M. Van Osch, H. Weinans and D. L. Bader, *Biochim. Biophys. Acta, Gen. Subj.*, 2002, **1570**, 1–8.
- 45 A. C. Rowat, J. Lammerding and J. H. Ipsen, *Biophys. J.*, 2006, **91**, 4649–4664.

- 46 J. D. Tice, H. Song, A. D. Lyon and R. F. Ismagilov, *Langmuir*, 2003, **19**, 9127–9133.
- 47 M. Glaubitz, N. Medvedev, D. Pussak, L. Hartmann, S. Schmidt, C. A. Helm and M. Delcea, *Soft Matter*, 2014, **10**, 6732–6741.
- 48 L. Latonen, *AIMS Mol. Sci.*, 2015, **2**, 324–331.
- 49 J. Lammerding, K. N. Dahl, D. E. Discher and R. D. Kamm, *Methods Cell Biol.*, 2007, **83**, 269–294.
- 50 T. Fischer, A. Hayn and C. T. Mierke, *Front. Cell Dev. Biol.*, 2020, **8**, 393.
- 51 J. Lammerding, L. G. Fong, J. Y. Ji, K. Reue, C. L. Stewart, S. G. Young and R. T. Lee, *J. Biol. Chem.*, 2006, **281**, 25768–25780.
- 52 L. Liu, Q. Luo, J. Sun, A. Wang, Y. Shi, Y. Ju, Y. Morita and G. Song, *Exp. Cell Res.*, 2017, **355**, 172–181.
- 53 R. S. Ryback, M. J. Eckardt, R. R. Rawlings and L. S. Rosenthal, *JAMA*, 1982, **248**, 2342–2345.
- 54 J. H. Friedman, *J. Am. Stat. Assoc.*, 1989, **84**, 165–175.
- 55 M. Lekka, *Bionanoscience*, 2016, **6**, 65–80.